# Forming ultracold YbAg molecules via photoassociation predicted from *ab initio* calculations

Xiang Yuan *

*Université de Lille, CNRS, UMR 8523–PhLAM–Physique des Lasers, Atomes et Molécules, F-59000 Lille, France and Department of Chemistry and Pharmaceutical Science, Faculty of Science, Vrije Universiteit Amsterdam, de Boelelaan 1083, 1081 HV Amsterdam, The Netherlands.*

Yong Liu

*School of Physics and Electronic Information, Yantai University, Yantai 264005, China*

(Received 15 December 2023; revised 1 December 2024; accepted 3 December 2024; published 17 December 2024)

This paper discusses the formation of ultracold YbAg molecules via photoassociation, following the proposal of using YbAg as a promising molecular candidate for electron electric dipole moment experiments [M. Verma *et al.* Phys. Rev. Lett. **125**, 153201 (2020)]. Our study utilizes high-level *ab initio* calculations, encompassing both multireference configuration interaction, relativistic Fock-space coupled cluster, and Kramers-restricted configuration interaction methods, to investigate the electronic structures including potential energy curves, spectroscopic constant, vibrational energy levels, and associated transition dipole moment and Franck-Condon factors for 28 electronic states. By choosing $(5)(\Omega = 3/2)$ as the intermediate state, we discuss the feasibility of forming ultracold YbAg molecules through stimulated Raman adiabatic passage method.

DOI: 10.1103/PhysRevA.110.062813

## I. INTRODUCTION

High-precision measurements of atoms and molecules now serve as invaluable tools to search for new physics beyond the standard model [1,2]. While the conventional approach to exploring violations of time-reversal symmetry involves searching for new particles at TeV-scale masses or higher, an alternative strategy focuses on highly accurate measurements of the electron electric dipole moment (eEDM) in atoms and molecules. The latter method can be conducted on much lower energy scales [1,3].

Polar heavy molecules have a considerable advantage in eEDM experiments due to their intense internal relativistic electric fields. Such intense fields make the potential effects of a nonzero eEDM more discernible and detectable [4]. Recently Arrowsmith-Kron *et al.* [2] reviewed searching fundamental symmetries in molecules containing heavy radioactive elements. Precision is paramount in eEDM experiments because the expected value of the eEDM is incredibly small. The ultracold molecules are good candidates for such experiments, because the corresponding thermal motion of molecules is minimized, allowing for more precise measurements.

Laser cooling is a technique employed to reduce the velocity (and thus the kinetic energy) of particles by irradiating them with lasers. This method has revolutionized the field of atomic physics, enabling the production of ultracold samples [5–14]. Although direct laser cooling has been significantly advanced on molecular systems, including diatomic molecules (SrF [15], YO [16], CaF [17], and YbF [18]) as well as polyatomic molecules (SrOH [19], YbOH [20], and $CaOCH_3$ [21]), this method remains restrictive due to strict criteria for optical cycling [22,23]. Many molecules have complex energy levels, leading them to leak out of the cooling cycle. Alternatively, the production of cold molecules through photoassociation, which is based on cold atoms, offers a more flexible approach, accommodating various electronic structures of molecular candidates [24].

Verma *et al.* [25] proposed YbAg to be the next generation of molecular candidates for eEDM experiments. Very recently, Polet *et al.* [26] calculated the enhancement factors and concluded that the values are similar to other systems currently investigated experimentally to search spatial and time-reversal violating effects. YbAg is particularly suitable for the photoassociation method, as the cooling and trapping of Yb [27] and Ag atoms [28] was achieved in the early 2000s. Moreover, photoassociation techniques have been used successfully in the production of ultracold Yb-alkali metal molecules such as YbLi [29], YbRb [30], and YbCs [31].

We also note that the recent proposal has identified the isoelectronic RaAg molecule [32–34] as a promising candidate for eEDM experiments. This is partially driven by the successful demonstration of laser cooling and trapping of radium [35]. Additionally, RaAg is expected to exhibit advantageous characteristics in eEDM experiments [34]. However, no experiments have yet been reported on assembling RaAg from cold atoms, and challenges may emerge due to its radioactive decay and the resultant heating effect [36], which may complicate the pairing of cold atoms.

To design a photoassociation scheme for the experiment, it is essential to understand the molecular electronic structure including the potential energy curves (PECs) and the transition properties. Although Ag's electronic structure bears similarities to that of alkali-metal atoms, and the interaction between Yb and the alkali-metal atom has been studied [37–45], most

*Contact author: xiang.yuan@univ-lille.fr

 

researches only centered on the ground state. Furthermore, when forming molecules, Ag presents a more intricate electronic structure than alkali-metal atoms due to the presence of $4d$ inner shell electrons [46–51].

To the best of our knowledge, only Tomza [52] and Polet *et al.* [26] have studied the ground state of YbAg by performing the coupled cluster calculations. Currently, neither experimental measurement nor theoretical calculation research has been reported on the electronic structure of excited states.

In this study, we have two primary objectives: First, we need to benchmark earlier calculations on the ground state. Second, we evaluate the excited states and transition properties and discuss the associated photoassociation scheme.

Throughout this paper, we employ the multireference configuration interaction (MRCI) method to calculate both ground and excited states. Our calculations account for the core-valence and the spin-orbit coupling (SOC) effect, the latter is evaluated by the coupling between spin-free states. Additionally, we also perform relativistic Fock-space coupled cluster and Kramers-restricted configuration interaction calculations on the ground state to cross-check the MRCI+SOC results.

This paper is organized as follows: The calculation details are described in Sec. II. The obtained results are presented and discussed in Sec. III. Finally, a brief summary is presented in Sec. IV.

## II. COMPUTATIONAL DETAILS

We employ the MRCI calculations using the quantum chemistry program MOLPRO [53,54]. The process involves three steps:

(i) An initial Hartree-Fock calculation provides a single-configuration wave function as a starting point.

(ii) Next, the molecular orbitals are optimized through the complete active space self-consistent field (CASSCF) method [55,56].

(iii) The dynamic correlations are then assessed using the internally contracted multireference configuration interaction (icMRCI) [57,58]. To address size-extensivity, we apply the Davidson correction (+Q) [59,60].

A pivotal step in the CASSCF and MRCI calculations is the determination of an appropriate active space, which needs the balance between accuracy and computational cost. We explore the influence of active spaces on molecular dissociation and the bound region by conducting calculations on isolated atoms and the molecular ground state, respectively.

The relativistic effects include two parts: scalar relativistic effects, which are considered through the Douglas-Kroll-Hess one-electron integrals [61] and the SOC effects. The latter is addressed as a perturbation, determined by combining the Breit-Pauli operator and *state-interacting* method [62]. The $\Omega$ states are obtained by diagonalizing the total Hamiltonian matrix.

For the basis set, we choose the augmented correlation-consistent basis set aug-cc-pVTZ-DK for Ag [63] and aug-cc-pwCVTZ-DK3 for Yb [64].

The relativistic Fock-space coupled cluster (FSCC) [65] and Kramers-restricted configuration interaction (KRCI) [66–68] calculations are performed by the DIRAC program [69,70]. For both FSCC and KRCI calculations, we select the s-aug-dyall.v3z basis set for Yb [71] and Ag [72]. The Gaussian-type nucleus model [73] is utilized in calculations.

In FSCC calculations, we utilize the exact two-component molecular-mean-field (X2Cmmf) Hamiltonian [74], which can offer an accuracy very close to the parent four-component Hamiltonian. For simplification in subsequent discussions, we refer X2Cmmf to X2C. For FSCC, it starts from $YbAg^+$ and proceeds to the (0h,1p) sectors of Fock space. To avoid the so-called intruder states issues in FSCC, we employ the intermediate Hamiltonian approach [75,76]. The model space contains 20 spinors.

In KRCI calculations, we employ the four-component Dirac-Coulomb Hamiltonian with the usual approximation of the small-small component integrals by a Coulombic correction [77] (KRCI module employed in our calculations does not support the use of two-component Hamiltonians X2Cmmf). For the current calculation, we utilize the generalized active space as defined in the context of the RaAg calculation [34]. The detailed model space is illustrated in Fig. 1 of the Supplemental Material (SM) Ref. [78].

Based on the potential energy curves, we evaluate three spectroscopic constants: excitation energy $T_e$, equilibrium internuclear distance $R_e$, and vibrational constants $\omega_e$ for the bound states by the LEVEL program [79]. The dissociation energy $D_e$ is obtained by subtracting the energy at the point of $R_e$ from the energy at point of extensive separation. Finally, we calculate the transition properties, including permanent dipole moments (PDMs), transition dipole moments (TDMs), Franck-Condon factors (FCFs), and Einstein emission coefficients ($A_{v'v''}$).

## III. RESULT AND DISCUSSION

### A. Atomic calculation

For Yb, we adopted two active spaces: one focuses solely on the valence orbitals $6s6p$, while another additionally incorporates the $7p$ orbitals. For Ag, the active space encompassed the valence orbitals $5s5p$. The inclusion of core orbitals is crucial for heavy elements due to their pronounced interactions that cannot be ignored in precise calculations. However, fully correlating core electrons in MRCI can become prohibitively expensive. Therefore, we incorporate the inner shells $4f$ of Yb and $4d$ of Ag into the calculations, ensuring that these orbitals remain doubly occupied in all reference configurations. These orbitals are then correlated using single and double excitations within the CI calculation. The results of Yb and Ag are detailed in Tables I and II, respectively.

We note that fully relativistic KRCI calculation underestimated the average energy of $^3P^o$, but accurately captured energy splitting between its substates. We attribute this underestimation to the limitations in virtual orbital space.

On the other hand, the current MRCI + SOC method yielded a more accurate average energy for $^3P^o$ state and slightly underestimated the splitting energy between $^3P_0^o$ and $^3P_1^o$. The $7p$ orbital plays a crucial role in capturing the spin-orbit coupling effect. As shown in the results of the first two rows in Table I, including the $7p$ orbital increase the spin-orbit

TABLE I. The energy ($cm^{-1}$) of $(6s6p)\,^3P^o$ and the associated three spin-orbit substates of Yb.

| | $^3P^o$ | $^3P^o_0$ | $^3P^o_1$ | $^3P^o_2$ | $(^3P^o_1 - ^3P^o_0)$ | $(^3P^o_2 - ^3P^o_0)$ |
|---|---|---|---|---|---|---|
| MRCI[a] | 16 984 | 15 543 | 16 127 | 17 787 | 584 | 2244 |
| MRCI[b] | 16 882 | 15 262 | 15 973 | 17 752 | 711 | 2490 |
| KRCI[c] | 15 475 | 14 038 | 14 713 | 16 221 | 675 | 2183 |
| FSCC | 18 057 | 16 332 | 17 135 | 18 955 | 802 | 2623 |
| Cal[d] | 20 119 | | | | | |
| Cal[e] | 19 836 | 18 249 | 18 946 | 20 688 | 700 | 2439 |
| Exp[f] | 18 868 | 17 288 | 17 992 | 19 710 | 704 | 2422 |

[a]Active space: $6s6p$
[b]Active space: $6s6p$+$7p$
[c]dyall.v4z basis set
[d]CCSD(T) [52].
[e]CI+MBPT [80].
[f]Experimental value from NIST.

splitting energy between $^3P^o_0$ and $^3P^o_1$ from 584 to 711 $cm^{-1}$, which is in close agreement with the experimental value of 704 $cm^{-1}$. For the results of Ag, the deviations between our computed spin-orbit substate values and the experimental values are within 200 $cm^{-1}$.

The relativistic FSCC calculations demonstrate similar accuracy in capturing both electron correlation and spin-orbit coupling effects. For example, the spin-orbit splitting of $(^2P^o_{3/2} - ^2P^o_{1/2})$ of Ag differs from the experimental results by a mere 16 $cm^{-1}$.

### B. Molecular ground state

The calculations of isolated atoms characterized the wave function in the molecular dissociation region. In this section, we focus on the ground state of YbAg, shedding light on the wave function within the bound region. In the molecular calculation, the $C_{2v}$ point group that is the Abelian subgroup of the $C_{\infty v}$ point group is employed. The corresponding relationships between the reducible representations of two point groups are $\Sigma^+ = A1$, $\Sigma^- = A2$, $\Pi = B1 + B2$, and $\Delta = A1 + A2$ respectively.

To elucidate the impact of the inner shell electrons, two sets of calculations are established: First, we correlate only valence orbitals. Second, we incorporate the inner shell orbitals of $4f$ (for Yb) and $4d$ (for Ag), which are correlated exclusively during the CI calculations. The PECs of different models for the ground state are depicted in Fig. 1, and the

TABLE II. The energy ($cm^{-1}$) of $(5p)\,^2P^o$ and the associated two spin-orbit substates of Ag.

| | $^2P^o$ | $^2P^o_{1/2}$ | $^2P^o_{3/2}$ | $(^2P^o_{3/2} - ^2P^o_{1/2})$ |
|---|---|---|---|---|
| MRCI | 29 491 | 28 995 | 29 739 | 744 |
| FSCC | 29 914 | 29 311 | 30 216 | 905 |
| Cal[a] | 30 363 | | | |
| Exp[b] | 30 166 | 29 552 | 30 473 | 921 |

[a]CCSD(T) [52].
[b]Experimental value from NIST.

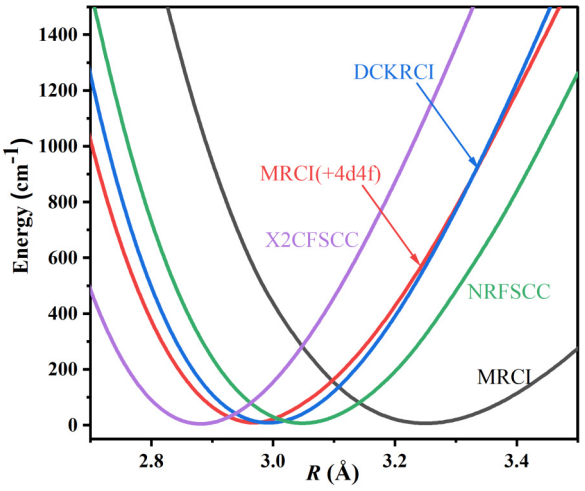


FIG. 1. The potential energy curves of the ground state in different calculation models.

corresponding equilibrium internuclear distance $R_e$ (Å) and vibrational constant $\omega_e$ ($cm^{-1}$) are listed in Table III.

From the MRCI results, we observe that the inner shell electrons have a substantial influence on the internuclear distance, causing a reduction in $R_e$ by 0.272 Å. The SOC appears to exert a minor effect on $R_e$, altering it by just $R_e$ by 0.003 Å. This can be attributed to the dominated electronic configuration of $\sigma_2\sigma_1^*$ which has minimal spin-orbit splitting. Compared to the KRCI calculation, we note the $R_e$ and $\omega_e$ values deviate from the results of the four-component calculations by only 0.021 Å and 3 $cm^{-1}$, respectively.

However, MRCI + SOC $R_e$ deviates from the recent CCSD(T) value reported by Tomza [52] 0.093 Å. The deviation of $R_e$ has significant effects on the transition property such as the Franck-Condon factor, which would result in different photoassociation schemes. We note that in the CCSD(T) calculation, Tomza [52] used an effective core potential (ECP) to describe the inner shell electrons in Yb, but explicitly correlated the $4d$ electrons of Ag. On the other hand, in our calculation, we find the $4f$ electrons of Yb have similar orbital energy to the $4d$ electrons of Ag, and they should be taken into account equally.

We perform both relativistic (X2C) and nonrelativistic (NR) FSCC calculations to investigate the effects of relativistic correction on the internuclear distance. The $R_e$ of NRFSCC and X2CFSCC are 3.042 Å and 2.871 Å, respectively, the

TABLE III. Spectroscopic constants of the $X^2\Sigma^+$ state of YbAg.

| Method | $R_e$(Å) | $\omega_e$($cm^{-1}$) |
|---|---|---|
| MRCI | 3.245 | 75.4 |
| MRCI(+$4d4f$) | 2.973 | 101.0 |
| MRCI(+$4d4f$)+SOC | 2.970 | 101.8 |
| DCKRCI | 2.991 | 104.9 |
| CCSD(T)[a] | 3.063 | 109.4 |
| NRFSCC | 3.042 | 96.7 |
| X2CFSCC | 2.871 | 110.7 |

[a]Reference [52].

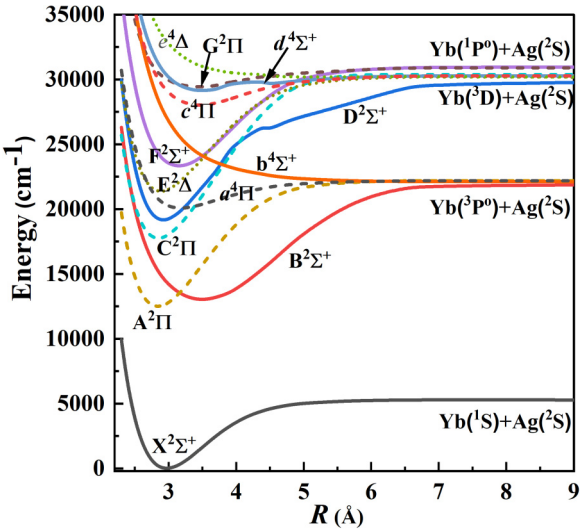


FIG. 2. The potential energy curves of 13 Λ-S state of YbAg molecule.

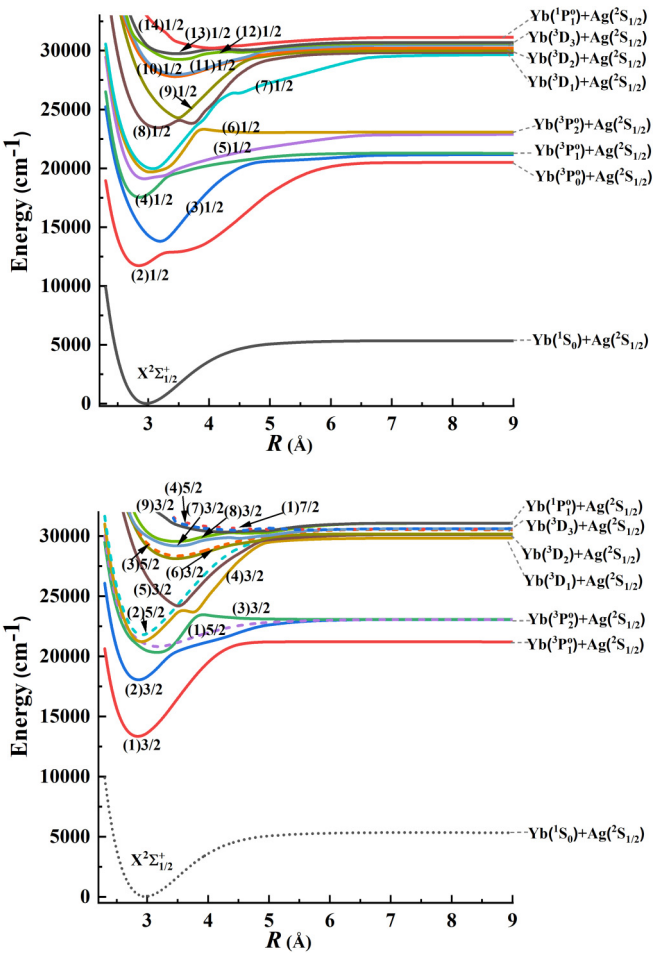


FIG. 3. The potential energy curves of 28 Ω states of YbAg molecule.

former is close to the CCSD(T) value of 3.063 Å. The FSCC calculations indicate the relativistic effects significantly reduce $R_e$ by 0.171 Å. Given the modesty SOC effect observed in the MRCI calculation, we attribute the relativistic corrections to the scalar relativistic effect of the inner shell electrons.

Based on atomic tests and molecular calculations on the ground state, we have determined the suitable active orbital space: 5$a$1, 2$b$1, 2$b$2, and 1$a$2 molecular orbitals in $C_{2v}$ symmetry corresponding to 6$s$, 6$p$, and 5$d$ orbitals of Yb and the 5$s$ orbital of Ag. (The 5$d$ orbital of Yb is included to facilitate the calculation of the $^3D$ state, which is discussed below). These orbitals are optimized and correlated in the CASSCF and CI steps. Meanwhile, the 4$f$ orbitals of Yb and the 4$d$ orbitals of Ag are correlated in the CI step without optimization. This orbital space should aptly describe the wave function in both the bound and dissociation regions and will serve as the basis for calculating other molecular excited states in subsequent discussions.

### C. Molecular excited states

As shown in Fig. 2, we calculated 13 Λ-S states, which correspond to the four lowest dissociation limits: Yb($^1S$)+Ag($^2S$) is related to the ground state as we extensively discussed in the last section. The second dissociation limit Yb($^3P^o$)+Ag($^2S$) corresponds to four Λ-S states including two doublet states $A^2\Pi$, $B^2\Sigma^+$, and two quartet states $a^4\Pi$, $b^4\Sigma^+$. Notably, the two doublet states both feature a deep potential well. However, quartet states exhibit less stability compared to doublet states. This is particularly evident in the $b^4\Sigma^+$ state, which is repulsive. The third dissociation limit Yb($^3D$)+Ag($^2S$) corresponds to six Λ-S states including three doublet states $E^2\Delta$, $C^2\Pi$, $D^2\Sigma^+$, and three quartet states $e^4\Delta$, $c^4\Pi$, $d^4\Sigma^+$. The two highest doublet states $G^2\Pi$ and $F^2\Sigma^+$, are associated with the fourth limit, Yb($^1P^o$)+Ag($^2S$). After considering SOC, we obtained 28 Ω states, including 14 states with $\Omega = 1/2$, 9 states with $\Omega = 3/2$, 4 states with $\Omega = 5/2$, and 1 state with $\Omega = 7/2$, corresponding to eight dissociation limits. The detailed dissociation relationships for the Ω states are presented in Table IV. The calculated dissociation limits align with the experimental values. We note that the lowest three dissociation limits are 2000 cm$^{-1}$ lower than the experimental value, consistent with observations from atomic tests above. On the other hand, by including the full *5d* shell of Yb in the active space, we reproduce three complete and accurate dissociation limits corresponding to the $^3D$ state. The PECs of Ω states are present in Fig. 3. It can be seen from the figure that the SOC effect results in several avoided crossing points among the Ω states, especially for the $\Omega = 1/2$ states. For instance, we note an avoided crossing point between the (2)1/2 and (3)1/2 states at 3.2 Å, which stems from the intersection between the $A^2\Pi$ and $B^2\Sigma^+$ states. Such avoided crossing can alter the shape of the PECs, as well as impact transition properties, such as Franck-Condon factors. The PDMs of the Ω state as a function of the internuclear distance are present in Fig. 4. The positive direction in the computation extends from Yb to Ag. The PDMs of $X^2\Sigma^+_{1/2}$ at $R_e$ is 0.76 a.u., which is smaller than the CCSD(T) value 1.30 a.u. reported in Ref. [52]. It can be seen that all the calculated PDMs at large internuclear distances are close to zero a.u. corresponding fact that all dissociation limits are neutral atoms. We also observe pronounced interactions between Ω states in the PDM curves. For instance, we observe two discontinuities in

TABLE IV. The dissociation relationship of the Ω states.

| Atomic State (Yb+Ag) | Ω States | Energy($cm^{-1}$) Cal. | Exp. |
|---|---|---|---|
| $^1S_0 + {}^2S_{1/2}$ | $X^2\Sigma^+_{1/2}$ | 0.0 | 0.0 |
| $^3P^o_0 + {}^2S_{1/2}$ | (2)1/2 | 15 124 | 17 288 |
| $^3P^o_1 + {}^2S_{1/2}$ | (1)3/2, (3)1/2, (4)1/2, | 15 859 | 17 992 |
| $^3P^o_2 + {}^2S_{1/2}$ | (1)5/2, (2)3/2, (3)3/2, (5)1/2, (6)1/2 | 17 751 | 19 710 |
| $^3D_1 + {}^2S_{1/2}$ | (4)3/2, (7)1/2, (8)1/2 | 24 484 | 24 489 |
| $^3D_2 + {}^2S_{1/2}$ | (2)5/2, (5)3/2, (6)3/2, (9)1/2, (10)1/2 | 24 842 | 24 752 |
| $^3D_3 + {}^2S_{1/2}$ | (1)7/2, (3)5/2, (4)5/2, (8)3/2, (7)3/2, (11)1/2, (12)1/2 | 25 391 | 25 271 |
| $^1P^o_1 + {}^2S_{1/2}$ | (9)3/2, (13)1/2, (14)1/2, | 25 736 | 25 068 |

the (7)1/2 state: The first one, located around 3.0 Å, associates with the avoided crossings between the (7)1/2 and (6,5,4)1/2 states; the second, positioned at 3.6 Å, corresponds to the interaction with (6,8)1/2 state.

Based on the PECs, the spectroscopic constants of the bound Ω states including $R_e$, $\omega_e$, $T_e$, and $D_e$ are calculated and listed in Table V. For the ground state, which is well separated from other excited states, the associated nondiagonal SOC matrix elements $\langle X^2\Sigma^+|\hat{H}_{SO}|\Psi\text{exc}\rangle$ are small. This leads to modest changes in the spectroscopic constants, as observed in the $R_e$ and $\omega_e$ values. The $D_e$ value of the spin-orbit state $X^2\Sigma^+_{1/2}$ and spin-free state $X^2\Sigma^+$ are 5248 and 5197 $cm^{-1}$, respectively, both close to the CCSD(T) value 5253 $cm^{-1}$ [52].

While the SOC effect is not significant for the ground state, it becomes crucial for the excited states. For example, under SOC, the $A^2\Pi$ state is split into (2)1/2 and (1)3/2 states with a splitting energy of 1622 $cm^{-1}$. For the (3)1/2 state, combing the SOC and the avoided crossing with $A^2\Pi$ state, we note the $R_e$ and $T_e$ are 3.198 Å and 13 739 $cm^{-1}$. These values deviate from those of the Λ-S state $B^2\Sigma^+$ −0.29 Å and 759 $cm^{-1}$, respectively.

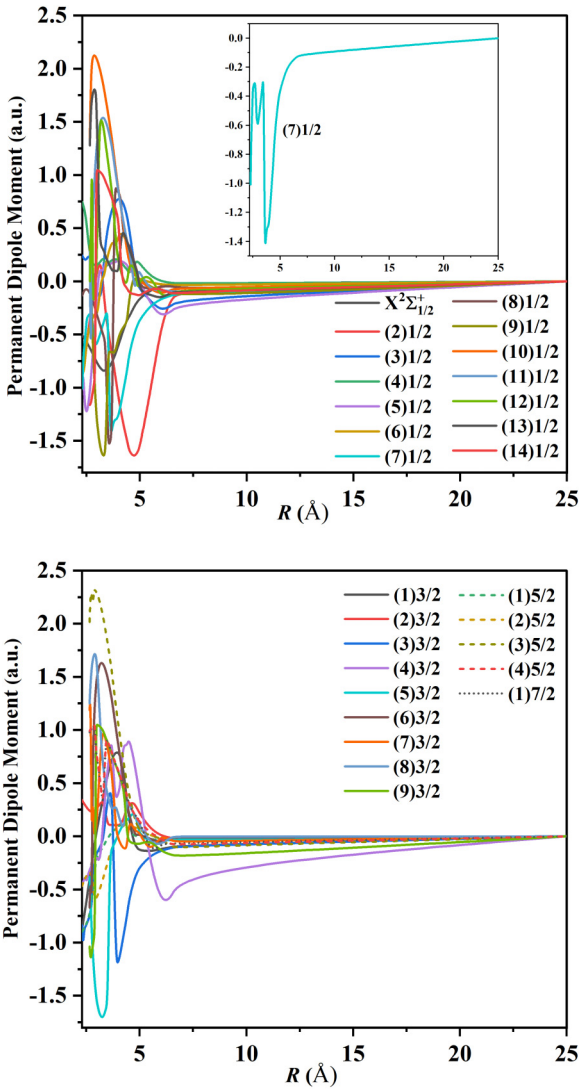


FIG. 4. The permanent dipole moment of 28 Ω states of YbAg molecule.

### D. Transition properties and photoassociation

In this section, we discuss the transition properties between ground and excited states. Given that the symmetry of the ground state is $\Omega = 1/2$, the states that allow electric dipole transition include $\Omega = 1/2$ and $\Omega = 3/2$. We show the

TABLE V. Spectroscopic constants of the Ω states.

| State | $R_e$ (Å) | $\omega_e$ ($cm^{-1}$) | $T_e$ ($cm^{-1}$) | $D_e$ ($cm^{-1}$) |
|---|---|---|---|---|
| $X^2\Sigma^+$ | 2.973 | 101.0 | 0 | 5197 |
| $X^2\Sigma^+_{1/2}$ | 2.970 | 101.8 | 0 | 5248 |
| (2)1/2 | 2.843 | 119.6 | 11 717 | 8658 |
| (3)1/2 | 3.198 | 135.1 | 13 739 | 7359 |
| (4)1/2 | 2.855 | 121.0 | 17 531 | 3604 |
| (5)1/2 | 2.932 | 82.7 | 19 104 | 3896 |
| (6)1/2 | 3.036 | 93.0 | 19 653 | 3332 |
| (7)1/2 | 3.087 | 121.0 | 19 919 | 9736 |
| (8)1/2 | 3.152 | 92.1 | 23 421 | 6226 |
| (9)1/2 | 3.493 | 177.0 | 24 179 | 5820 |
| (1)3/2 | 2.841 | 115.7 | 13 339 | 7761 |
| (2)3/2 | 2.855 | 118.3 | 18 041 | 4954 |
| (3)3/2 | 3.155 | 77.8 | 20 310 | 2686 |
| (4)3/2 | 2.903 | 126.6 | 21 210 | 8676 |
| (5)3/2 | 3.510 | 165.5 | 24 102 | 5886 |
| (6)3/2 | 3.449 | 61.3 | 28 116 | 2012 |
| (1)5/2 | 3.171 | 67.9 | 20 807 | 2186 |
| (2)5/2 | 2.914 | 126.3 | 21 780 | 8351 |

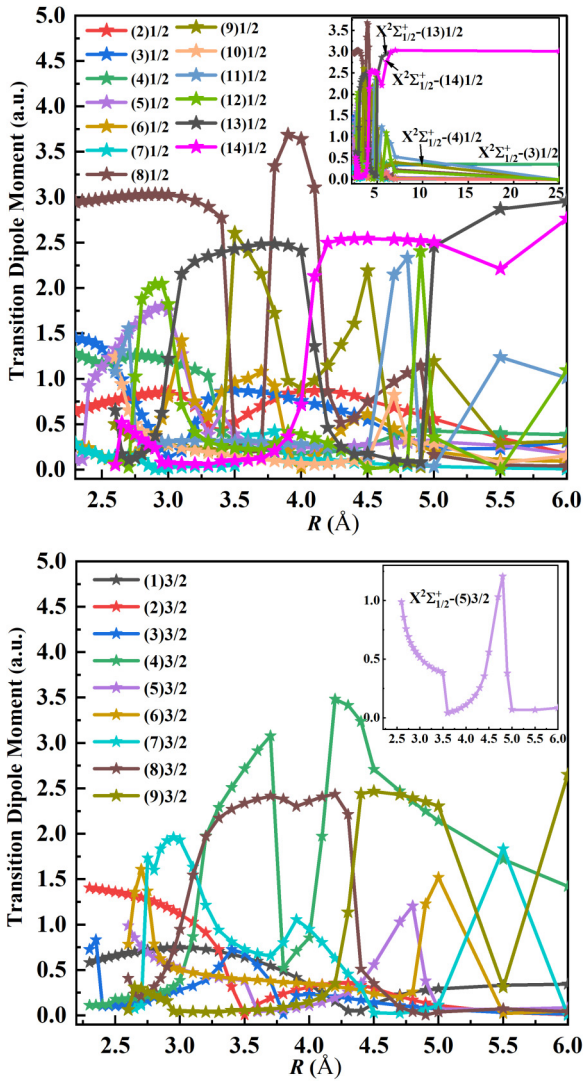


FIG. 5. Transition dipole moment between the ground state $X^2\Sigma^+_{1/2}$ and excited states.

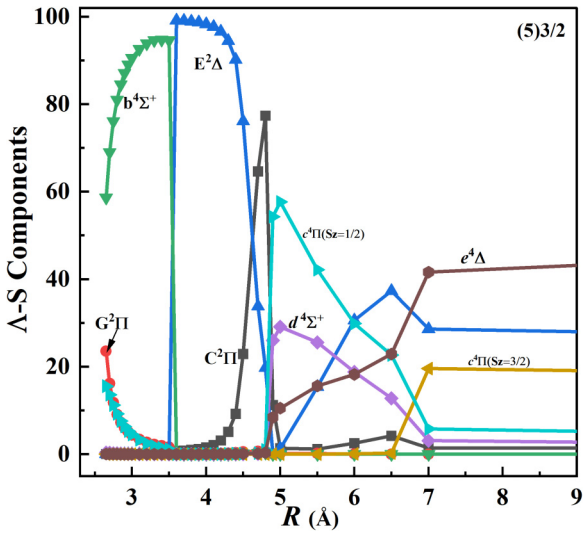


FIG. 6. Curves of Λ-S components versus $R$ of (5)3/2 states.

corresponding TDMs as a function of internuclear distance in Fig. 5. We observe significant oscillations for TDM mirroring the findings observed for PDM in Fig. 4. These oscillations underscore strongly avoided crossings among excited states, especially within the range from 3.5 to 5.0 Å. For example, we find that in the region of small nuclear distances, the TDM of $X^2\Sigma^+_{1/2}$ to (5)3/2 is nearly 1.0 (a.u.), then it decreases to zero at $R = 3.5$ Å and quickly approaches pole at $R = 4.5$ Å. This pole results from the avoided crossing between (5)3/2 and (4)3/2 states as shown above.

To further analyze the pole, we present the curves of Λ–S components versus $R$ for the (5)3/2 states in Fig. 6 (the Λ-S components curves for other Ω states are available in SM). Initially, the (5)3/2 state is dominated by the quartet state $b^4\Sigma^+$ and doublet state $G^2\Pi$, and the corresponding TDM to the ground state $X^2\Sigma^+$ is attributed from $G^2\Pi$ state as the transition to $b^4\Sigma^+$ being spin-forbidden. At $R = 3.5$ Å, the TDM is almost zero since the doublet state $E^2\Delta$ dominates the contribution and the associated transition $\Sigma \rightarrow \Delta$ is forbidden. At $R = 4.5$ Å, the second avoided crossing occurs where the $E^2\Delta$ is replaced by the doublet state $C^2\Pi$, which allows a spin-allowed transition to the ground state. In the dissociation region, the TDM clearly converges towards the atomic transition of Yb. For instance, among the 14 ($\Omega = 1/2$) states, only (3,4)1/2 and (13,14)1/2 states remain nonzero when $R$ approaches the dissociation limits. This is because the other states either belong to $^3P^o$ substates $^3P^o_0$ and $^3P^o_2$, whose transition to $^1S_0$ are forbidden by selection rule, or to the $^3D$ state, where transitions to $^1S_0$ are parity forbidden.

Notably, the TDM of (3,4)1/2 states are significantly smaller than that of (13,14)1/2 as the former corresponds to the triplet to singlet transition from $^3P^o_1$ to $^1S_0$, while the latter is associated with a single to singlet transition from $^1P^o_1$ to $^1S_0$, which is a spin-allowed transition. The TDM value for the (3)1/2 state, 0.37 a.u. at $R = 25$ Å, is consistent with the previous atomic calculation, which yielded 0.33 a.u. [81].

Beyond electronic transitions, we also assess transitions between vibrational wave functions by determining the Franck-Condon factors $q_{v'v''}$. FCFs describe the coupling of vibrational wave functions of the ground and excited electronic states. We collect the vibrational energy levels of each excited state in Table I of SM. Our primary focus is to make the systems occupying the lowest vibrational level of the ground state [$X^2\Sigma^+_{1/2}(v'' = 0, J = 0)$, $J$ is the rotational quantum number]. We tabulate the FCFs between excited states and $X^2\Sigma^+_{1/2}(v'' = 0, J = 0)$ in Table VI, while the transitions to the higher vibrational energy levels of the ground state are detailed in Table II of SM. From Table VI, we find the (5)1/2($v' = 0$) state has the largest FCF value of 0.908, which can be understood by noting that the $R_e$ of (5)1/2 state deviates from that of ground state only 0.038 Å.

By using the vibrationally averaged transition dipole moment $\mathrm{TDM}_{v',v''}$, we evaluate the Einstein emission coefficients $A_{v',v''}$ (in $s^{-1}$) for excited states with the equation [82]:

$$A_{v'v''} = 2.142 \times 10^{10} \times \mathrm{TDM}^2_{v',v''} \times \Delta E^3 \qquad (1)$$

where the energy difference $\Delta E$ and $\mathrm{TDM}_{v',v''}$ are given in a.u.

TABLE VI. FCFs $q_{v'0}$ of the YbAg molecule between excited states and lowest vibrational level of the ground state. Numerals in square brackets represent power of 10.

| | (2)1/2 | (3)1/2 | (4)1/2 | (5)1/2 | (9)1/2 |
|---|---|---|---|---|---|
| $v'=0$ | 1.85[−1] | 4.64[−3] | 2.31[−1] | 9.08[−1] | <1.0[−10] |
| 1 | 3.43[−1] | 2.56[−2] | 3.50[−1] | 8.67[−1] | <1.0[−10] |
| 2 | 2.82[−1] | 7.12[−2] | 2.54[−1] | 4.19[−3] | 7.48[−10] |
| 3 | 1.37[−1] | 1.29[−1] | 1.16[−2] | 4.41[−4] | 1.31[−8] |
| 4 | 4.33[−2] | 1.72[−1] | 3.77[−2] | 1.06[−3] | 1.24[−7] |
| 5 | 8.89[−3] | 1.81[−1] | 9.05[−3] | 3.85[−5] | 8.05[−7] |
| 6 | 1.10[−3] | 1.56[−1] | 1.65[−3] | 4.10[−5] | 4.03[−6] |
| | (1)3/2 | (2)3/2 | (3)3/2 | (4)3/2 | (5)3/2 |
| $v'=0$ | 1.72[−1] | 2.31[−1] | 5.74[−2] | 6.27[−1] | <1.0[−10] |
| 1 | 3.23[−1] | 3.51[−1] | 1.77[−1] | 2.95[−1 | <1.0[−10] |
| 2 | 2.80[−1] | 2.55[−1] | 2.67[−1] | 6.89[−2] | 1.16[−10] |
| 3 | 1.50[−1] | 1.16[−1] | 2.46[−1] | 8.71[−3] | 2.38[−9] |
| 4 | 5.56[−2] | 3.64[−2] | 1.54[−1] | 7.78[−4 | 2.94[−8] |
| 5 | 1.51[−2] | 8.23[−3] | 6.92[−2] | 6.25[−5 | 2.44[−7] |
| 6 | 3.21[−3] | 1.40[−3] | 2.25[−2] | 3.73[−6] | 1.47[−6] |

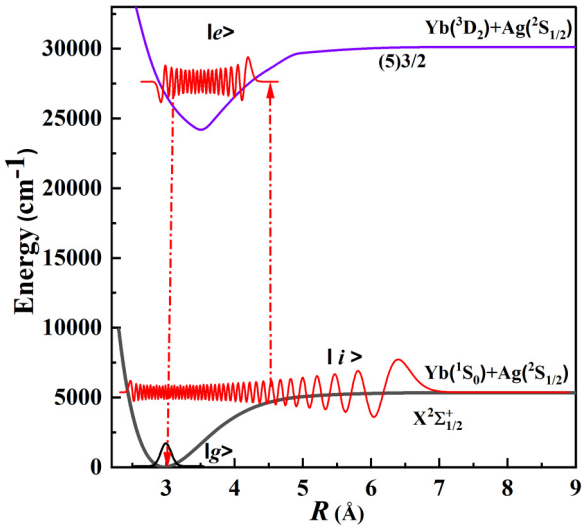


FIG. 7. STIRAP scheme for transferring the weakly bound state $|i\rangle$ to the rovibrational ground state $|g\rangle$ via the intermediate state $|e\rangle$ $v'=35$ in (5)3/2 state;

In Table VII, we present the $A_{v',v''}$ associated to the $X^2\Sigma^+_{1/2}(v''=0, J=0)$ state. Results corresponding to other vibrational levels are detailed in Table III of SM.

The diagonal feature of the FCFs for the (5)1/2 state may lead to a scheme of direct laser cooling, which is similar to what had been reported for KRb molecules [83]. Here we explore the application of the stimulated Raman adiabatic passage (STIRAP) method [84] to efficiently form YbAg molecules in the vibrational ground state $X^2\Sigma_{1/2}(v''=0, J=0)$.

The STIRAP technique offers significant benefits, including reduced losses and improved preparation efficiency. In Fig. 7, we utilize a two-photon, three-level model to illustrate our scheme. Initially, the system occupies the initial state $|i\rangle$, typically a weakly bound state. This initial state can be prepared using Narrow Feshbash resonances [85,86], or through mergoassociation [87]. Our target state for preparation is the lowest rovibrational state $|g\rangle$ $[X^2\Sigma_{1/2}(v''=0, J=0)]$. A critical aspect of the STIRAP method is the selection of an appropriate intermediate state $|e\rangle$. This choice significantly influences the formation of the dark state during the process, thereby mitigating the impact of the excited state and enhancing overall efficiency. To better gauge transfer efficiency, we adopt the approach proposed by Chen *et al.* [88] and define a function $F = q_{v',v''} \times q_{v',0}$ to quantify the product of the FCFs. This approach is particularly relevant because smaller FCFs typically necessitate higher laser intensities. For excited states with highly diagonal FCFs, such as the (5)1/2 state, the associated $F$ value is quite small. Here we discuss (5)3/2 state as our intermediate state, since its $F$ values can exceed $10^{-5}$ magnitude, which is large for the efficient preparation of ultracold molecules [88].

TABLE VII. Einstein coefficients $A_{v'0}$ (in $s^{-1}$) of the YbAg molecule. Numerals in square brackets represent power of 10.

| | (2)1/2 | (3)1/2 | (4)1/2 | (5)1/2 | (9)1/2 |
|---|---|---|---|---|---|
| $v'=0$ | 6.66[+4] | 2.03[+2] | 5.91[+5] | 6.08[+6] | 4.30[−8] |
| 1 | 1.28[+5] | 6.76[+3] | 8.97[+5] | 4.62[+5] | 4.76[−6] |
| 2 | 1.09[+5] | 1.28[+3] | 6.46[+5] | 7.05[+4] | 2.01[−4] |
| 3 | 5.41[+4] | 2.00[+3] | 2.94[+5] | 5.01[+1] | 3.75[−3] |
| 4 | 1.72[+4] | 3.09[+3] | 9.38[+4] | 1.17[+4] | 3.63[−2] |
| 5 | 3.45[+3] | 4.77[+3] | 2.21[+4] | 2.24[+3] | 2.37[−1] |
| 6 | 3.86[+2] | 6.69[+3] | 3.93[+2] | 3.69[+2] | 1.18[0] |
| | (1)3/2 | (2)3/2 | (3)3/2 | (4)3/2 | (5)3/2 |
| $v'=0$ | 7.06[+4] | 5.93[+5] | 1.51[+4] | 1.90[+5] | 3.76[−8] |
| 1 | 1.38[+5] | 8.71[+5] | 4.04[+4] | 1.52[+5] | 2.69[−6] |
| 2 | 1.23[+5] | 6.10[+5] | 5.69[+4] | 7.38[+4] | 9.76[−5] |
| 3 | 6.78[+4] | 2.65[+5] | 4.89[+4] | 2.83[+4] | 2.08[−3] |
| 4 | 2.56[+4] | 7.81[+4] | 2.86[+4] | 9.87[+3] | 2.66[−2] |
| 5 | 7.07[+3] | 1.64[+4] | 1.19[+4] | 2.72[+3] | 2.28[−1] |
| 6 | 1.51[+3] | 2.53[+3] | 3.53[+3] | 4.23[+2] | 1.42[0] |

We have scanned all initial vibrational states ($v''$ from 0 to 86) to evaluate the transfer efficiency. Figure 8 display the function $F$, representing the product of the Franck-Condon factors. These are plotted against the vibrational energy level $v''$ for the initial state and the vibrational energy level $v'$ for the intermediate state.

We can see in Fig. 8 that a more deeply bound initial vibrational state $v''$, correlates with a higher value $F$. For example, selecting $v''=45$ and $v'=26$ as $|i\rangle$ and $|e\rangle$, respectively, results in $F$ reaching the maximum value of $1.0\times10^{-2}$. This magnitude is comparable to those observed in the scheme for the NaCs molecule [89,90].

In the experiment, however, the system predominantly occupies the higher initial vibrational states just below the dissociation limit. When we use the (5)3/2 as the intermediate state (see Fig. 8), the product value $F$ can still reach $1.0\times10^{-5}$ even when utilizing a very high initial state. For instance, choosing $v''=84(v''=-2)$ as the initial state and choosing $v'=35$ as the intermediate state, the resulting $F$ value is $3.8\times10^{-5}$. The wavelength of the

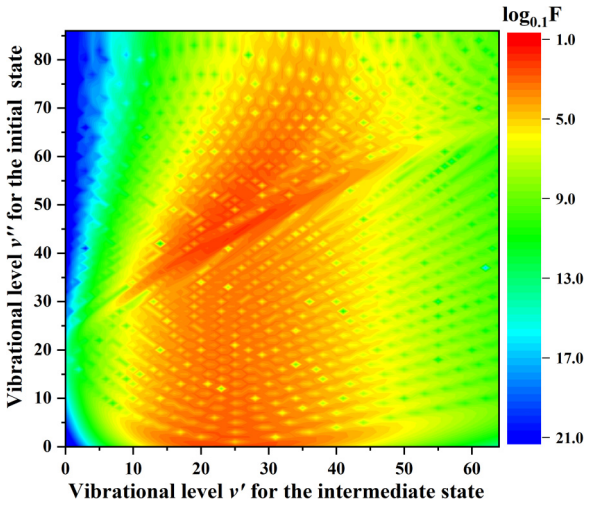


FIG. 8. Products of Franck-Condon factors between the initial ground vibrational level $v''$, the intermediate vibrational level $v'$ in the (5)3/2 state and the rovibrational ground state $X^2\Sigma_{1/2}(v''=0, J=0)$.

pump laser is 449 nm for the transition $X^2\Sigma^+_{1/2}(v''=84) \rightarrow (5)3/2(v'=35)$, falling within the visible spectrum, whereas the wavelength of the dump laser is 362 nm for transition $(5)3/2(v'=35) \rightarrow X^2\Sigma^+_{1/2}(v''=0)$, which is in the near ultraviolet spectrum. Based on the discussion above, we identify obtaining the high vibration levels (HVLs) of electronic states as a critical step for future STIRAP simulations and experiments. However, an accurate calculation of HVLs remains challenging, even for the ground state of a light molecule [91]. For YbAg, employing larger basis sets and higher-level Hamiltonians in future calculations could enhance the accuracy. While such extensive calculations currently exceed our computational capabilities, recent advancements in relativistic quantum chemistry-including Cholesky decomposition [92–94] and frozen natural orbitals [95–97] are expected to render these calculations feasible in near future.

## IV. CONCLUSION

In this work, we have investigated the electronic structure of YbAg molecules using high-level MRCI + SOC and relativistic FSCC, KRCI calculations.

First, we benchmark the previous calculations on the ground state and find that it is necessary to correlate the inner-shell electrons ($4f$ of Yb and $4d$ of Ag) in the calculations to adequately address the relativistic effects.

We have evaluated the potential energy curves of excited states corresponding to eight dissociation limits and derived the spectroscopic constants. We observed significant avoided crossings among the excited states. Furthermore, we evaluate the transition properties including transition dipole moment, Franck-Condon factors, and the Einstein emission coefficients (complete details are provided in SM [78].).

Finally, our discussion focuses on the use of the stimulated Raman adiabatic passage method by selecting the (5) ($\Omega = 3/2$) state as the intermediate state for the formation of ultracold YbAg molecules in the vibrational ground state $X^2\Sigma^+_{1/2}(v''=0, J=0)$. Our study provides a possible scheme that will stimulate future experimental research on the photoassociation of YbAg molecules.

## ACKNOWLEDGMENTS

X.Y. acknowledges funding from projects Labex CaPPA (ANR-11-LABX-0005-01) and CompRIXS (ANR-19-CE29-0019 and DFG JA 2329/6-1), the I-SITE ULNE project OVERSEE and MESONM International Associated Laboratory (LAI) (ANR-16-IDEX-0004), and support from the French national supercomputing facilities (Grant No. DARI A0090801859).

[1] M. S. Safronova, D. Budker, D. DeMille, D. F. Jackson Kimball, A. Derevianko, and C. W. Clark, Rev. Mod. Phys. **90**, 025008 (2018).
[2] G. Arrowsmith-Kron, M. Athanasakis-Kaklamanakis, M. Au, J. Ballof, R. Berger, A. Borschevsky, A. A. Breier, F. Buchinger, D. Budker, L. Caldwell *et al.*, Rep. Prog. Phys. **87**, 084301 (2024).
[3] T. E. Chupp, P. Fierlinger, M. J. Ramsey-Musolf, and J. T. Singh, Rev. Mod. Phys. **91**, 015001 (2019).
[4] L. I. Schiff, Phys. Rev. **132**, 2194 (1963).
[5] D. V. Seletskiy, R. Epstein, and M. Sheik-Bahae, Rep. Prog. Phys. **79**, 096401 (2016).
[6] C. Adams and E. Riis, Prog. Quantum Electron. **21**, 1 (1997).
[7] S. Stenholm, Rev. Mod. Phys. **58**, 699 (1986).
[8] S. Chu, Rev. Mod. Phys. **70**, 685 (1998).
[9] C. N. Cohen-Tannoudji, Rev. Mod. Phys. **70**, 707 (1998).
[10] W. D. Phillips, Rev. Mod. Phys. **70**, 721 (1998).
[11] W. Ketterle, Rev. Mod. Phys. **74**, 1131 (2002).
[12] N. Fitch and M. Tarbutt, Adv. At. Mol. Opt. Phys. **70**, 157 (2021).
[13] D. McCarron, J. Phys. B: At. Mol. Opt. Phys. **51**, 212001 (2018).
[14] F. Schreck and K. V. Druten, Nat. Phys. **17**, 1296 (2021).
[15] E. S. Shuman, J. F. Barry, and D. DeMille, Nature (London) **467**, 820 (2010).
[16] M. T. Hummon, M. Yeo, B. K. Stuhl, A. L. Collopy, Y. Xia, and J. Ye, Phys. Rev. Lett. **110**, 143001 (2013).
[17] V. Zhelyazkova, A. Cournol, T. E. Wall, A. Matsushima, J. J. Hudson, E. A. Hinds, M. R. Tarbutt, and B. E. Sauer, Phys. Rev. A **89**, 053416 (2014).
[18] J. Lim, J. R. Almond, M. A. Trigatzis, J. A. Devlin, N. J. Fitch, B. E. Sauer, M. R. Tarbutt, and E. A. Hinds, Phys. Rev. Lett. **120**, 123201 (2018).
[19] I. Kozyryev, L. Baum, K. Matsuda, B. L. Augenbraun, L. Anderegg, A. P. Sedlack, and J. M. Doyle, Phys. Rev. Lett. **118**, 173201 (2017).

[20] B. L. Augenbraun, Z. D. Lasner, A. Frenett, H. Sawaoka, C. Miller, T. C. Steimle, and J. M. Doyle, New J. Phys. **22**, 022003 (2020).

[21] D. Mitra, N. B. Vilas, C. Hallas, L. Anderegg, B. L. Augenbraun, L. Baum, C. Miller, S. Raval, and J. M. Doyle, Science **369**, 1366 (2020).

[22] M. D. Rosa, Eur. Phys. J. D **31**, 395 (2004).

[23] M. V. Ivanov, T.-C. Jagau, G.-Z. Zhu, E. R. Hudson, and A. I. Krylov, Phys. Chem. Chem. Phys. **22**, 17075 (2020).

[24] K. M. Jones, E. Tiesinga, P. D. Lett, and P. S. Julienne, Rev. Mod. Phys. **78**, 483 (2006).

[25] M. Verma, A. M. Jayich, and A. C. Vutha, Phys. Rev. Lett. **125**, 153201 (2020).

[26] J. D. Polet, Y. Chamorro, L. F. Pašteka, S. Hoekstra, M. Tomza, A. Borschevsky, and I. A. Aucar, arXiv:2408.15029.

[27] K. Honda, Y. Takahashi, T. Kuwamoto, M. Fujimoto, K. Toyoda, K. Ishikawa, and T. Yabuzaki, Phys. Rev. A **59**, R934 (1999).

[28] G. Uhlenberg, J. Dirscherl, and H. Walther, Phys. Rev. A **62**, 063404 (2000).

[29] A. Green, J. H. S. Toh, R. Roy, M. Li, S. Kotochigova, and S. Gupta, Phys. Rev. A **99**, 063416 (2019).

[30] N. Nemitz, F. Baumer, F. Münchow, S. Tassy, and A. Görlitz, Phys. Rev. A **79**, 061403(R) (2009).

[31] A. Guttridge, S. A. Hopkins, M. D. Frye, J. J. McFerran, J. M. Hutson, and S. L. Cornish, Phys. Rev. A **97**, 063414 (2018).

[32] T. Fleig and D. DeMille (2018), https://dirac.ups-tlse.fr/fleig/talks/Fleig_Mainz2019.pdf.

[33] M. Śmiałkowski and M. Tomza, Phys. Rev. A **103**, 022802 (2021).

[34] T. Fleig and D. DeMille, New J. Phys. **23**, 113039 (2021).

[35] J. R. Guest, N. D. Scielzo, I. Ahmad, K. Bailey, J. P. Greene, R. J. Holt, Z.-T. Lu, T. P. O'Connor, and D. H. Potterveld, Phys. Rev. Lett. **98**, 093001 (2007).

[36] M. Fan, *Radium Ions and Radioactive Molecules for Probing New Physics* (University of California, Santa Barbara, 2023).

[37] S. N. Tohme and M. Korek, Comput. Theor. Chem. **1078**, 65 (2016).

[38] S. N. Tohme and M. Korek, Chem. Phys. Lett. **638**, 216 (2015).

[39] S. Tohme and M. Korek, Chem. Phys. **410**, 37 (2013).

[40] S. N. Tohme, M. Korek, and R. Awad, J. Chem. Phys. **142**, 114312 (2015).

[41] Q. Shao, L. Deng, X. Xing, D. Gou, X. Kuang, and H. Li, J. Phys. Chem. A **121**, 2187 (2017).

[42] P. Zhang, H. R. Sadeghpour, and A. Dalgarno, J. Chem. Phys. **133**, 044306 (2010).

[43] L. K. Sørensen, S. Knecht, T. Fleig, and C. M. Marian, J. Phys. Chem. A **113**, 12607 (2009).

[44] D. A. Brue and J. M. Hutson, Phys. Rev. A **87**, 052709 (2013).

[45] G. Gopakumar, M. Abe, B. P. Das, M. Hada, and K. Hirao, J. Chem. Phys. **133**, 124317 (2010).

[46] J. Loreau, H. R. Sadeghpour, and A. Dalgarno, J. Chem. Phys. **138**, 084301 (2013).

[47] J. G. Hill and K. A. Peterson, J. Chem. Theory Comput. **8**, 518 (2012).

[48] X. Liu, L. McKemmish, and J. Pérez-Ríos, Phys. Chem. Chem. Phys. **25**, 4093 (2023).

[49] R. B. Ross and W. C. Ermler, J. Phys. Chem. **89**, 5202 (1985).

[50] C. Li, Y. Li, Z. Ji, X. Qiu, Y. Lai, J. Wei, Y. Zhao, L. Deng, Y. Chen, and J. Liu, Phys. Rev. A **97**, 062501 (2018).

[51] W. Zhou, Y. Zhao, G. Guo, X. He, T. Gong, X. Qiu, Y. Tian, X. Sun, S. Liu, J. Cai, B. Fiser, M. Szőri, C. Fittschen, A. Alijah, and C. Li, J. Mol. Struct. **1286**, 135524 (2023).

[52] M. Tomza, New J. Phys. **23**, 085003 (2021).

[53] H.-J. Werner, P. J. Knowles, F. R. Manby, J. A. Black, K. Doll, A. Heßelmann, D. Kats, A. Köhn, T. Korona, D. A. Kreplin, Q. Ma, T. F. Miller, A. Mitrushchenkov, K. A. Peterson, I. Polyak, G. Rauhut, and M. Sibaev, J. Chem. Phys. **152**, 144107 (2020).

[54] H.-J. Werner, P. J. Knowles, G. Knizia, F. R. Manby, and M. Schütz, WIREs Comput. Mol. Sci. **2**, 242 (2012).

[55] H.-J. Werner and P. J. Knowles, J. Chem. Phys. **82**, 5053 (1985).

[56] P. J. Knowles and H.-J. Werner, Chem. Phys. Lett. **115**, 259 (1985).

[57] H.-J. Werner and P. J. Knowles, J. Chem. Phys. **89**, 5803 (1988).

[58] P. J. Knowles and H.-J. Werner, Chem. Phys. Lett. **145**, 514 (1988).

[59] K. Jankowski, L. Meissner, and J. Wasilewski, Int. J. Quantum Chem. **28**, 931 (1985).

[60] S. R. Langhoff and E. R. Davidson, Int. J. Quantum Chem. **8**, 61 (1974).

[61] M. Reiher, Theor. Chem. Acc. **116**, 241 (2006).

[62] A. Berning, M. Schweizer, H.-J. Werner, P. J. Knowles, and P. Palmieri, Mol. Phys. **98**, 1823 (2000).

[63] K. A. Peterson and C. Puzzarini, Theor. Chem. Acc. **114**, 283 (2005).

[64] Q. Lu and K. A. Peterson, J. Chem. Phys. **145**, 054111 (2016).

[65] L. Visscher, E. Eliav, and U. Kaldor, J. Chem. Phys. **115**, 9720 (2001).

[66] T. Fleig, J. Olsen, and L. Visscher, J. Chem. Phys. **119**, 2963 (2003).

[67] T. Fleig, H. J. A. Jensen, J. Olsen, and L. Visscher, J. Chem. Phys. **124**, 104106 (2006).

[68] S. Knecht, H. J. A. Jensen, and T. Fleig, J. Chem. Phys. **132**, 014108 (2010).

[69] T. Saue, R. Bast, A. S. P. Gomes, H. J. A. Jensen, L. Visscher, I. A. Aucar, R. Di Remigio, K. G. Dyall, E. Eliav, E. Fasshauer, T. Fleig, L. Halbert, E. D. Hedegård, B. Helmich-Paris, M. Iliaš, C. R. Jacob, S. Knecht, J. K. Laerdahl, M. L. Vidal, M. K. Nayak, M. Olejniczak, J. M. H. Olsen, M. Pernpointner, B. Senjean, A. Shee, A. Sunaga, and J. N. P. van Stralen, J. Chem. Phys. **152**, 204104 (2020).

[70] DIRAC, a relativistic *ab initio* electronic structure program, Release DIRAC22 (2022), written by H. J. Aa. Jensen, R. Bast, A. S. P. Gomes, T. Saue and L. Visscher, with contributions from I. A. Aucar, V. Bakken, C. Chibueze, J. Creutzberg, K. G. Dyall, S. Dubillard, U. Ekström, E. Eliav, T. Enevoldsen, E. Faßhauer, T. Fleig, O. Fossgaard, L. Halbert, E. D. Hedegård, T. Helgaker, B. Helmich–Paris, J. Henriksson, M. van Horn, M. Iliaš, Ch. R. Jacob, S. Knecht, S. Komorovský, O. Kullie, J. K. Lærdahl, C. V. Larsen, Y. S. Lee, N. H. List, H. S. Nataraj, M. K. Nayak, P. Norman, G. Olejniczak, J. Olsen, J. M. H. Olsen, A. Papadopoulos, Y. C. Park, J. K. Pedersen, M. Pernpointner, J. V. Pototschnig, R. di Remigio, M. Repisky, K. Ruud, P. Sałek, B. Schimmelpfennig, B. Senjean, A. Shee, J. Sikkema, A. Sunaga, A. J. Thorvaldsen, J. Thyssen, J. van Stralen, M. L. Vidal, S. Villaume, O. Visser, T. Winther, S. Yamamoto and X. Yuan available at http://dx.doi.org/10.5281/zenodo.6010450, see also http://www.diracprogram.org.

[71] A. S. P. Gomes, K. G. Dyall, and L. Visscher, Theor. Chem. Acc. **127**, 369 (2010).
[72] K. G. Dyall, Theor. Chem. Acc. **117**, 483 (2007).
[73] L. Visscher and K. G. Dyall, At. Data Nucl. Data Tables **67**, 207 (1997).
[74] J. Sikkema, L. Visscher, T. Saue, and M. Iliaš, J. Chem. Phys. **131**, 124116 (2009).
[75] A. Landau, E. Eliav, Y. Ishikawa, and U. Kaldor, J. Chem. Phys. **113**, 9905 (2000).
[76] A. Landau, E. Eliav, Y. Ishikawa, and U. Kaldor, J. Chem. Phys. **115**, 6862 (2001).
[77] L. Visscher, Theor. Chem. Acc. **98**, 68 (1997).
[78] See Supplemental Material at http://link.aps.org/supplemental/10.1103/PhysRevA.110.062813 for FCFs, Einstein coefficients, and vibrational energy levels.
[79] R. J. Le Roy, J. Quant. Spectrosc. Radiat. Transfer **186**, 167 (2017).
[80] V. A. Dzuba and A. Derevianko, J. Phys. B: At. Mol. Opt. Phys. **43**, 074011 (2010).
[81] K. Blagoev and V. Komarovskii, At. Data Nucl. Data Tables **56**, 1 (1994).
[82] H. Okabe *et al.*, *Photochemistry of Small Molecules* (Wiley, New York, 1978), Vol. 431.
[83] J. Kobayashi, K. Aikawa, K. Oasa, and S. Inouye, Phys. Rev. A **89**, 021401(R) (2014).
[84] K. Bergmann, H. Theuer, and B. W. Shore, Rev. Mod. Phys. **70**, 1003 (1998).
[85] A. Green, H. Li, J. H. See Toh, X. Tang, K. C. McCormick, M. Li, E. Tiesinga, S. Kotochigova, and S. Gupta, Phys. Rev. X **10**, 031037 (2020).
[86] M. Tomza, F. Pawłowski, M. Jeziorska, C. P. Koch, and R. Moszynski, Phys. Chem. Chem. Phys. **13**, 18893 (2011).
[87] D. K. Ruttley, A. Guttridge, S. Spence, R. C. Bird, C. R. Le Sueur, J. M. Hutson, and S. L. Cornish, Phys. Rev. Lett. **130**, 223401 (2023).
[88] T. Chen, S. Zhu, X. Li, J. Qian, and Y. Wang, Phys. Rev. A **89**, 063402 (2014).
[89] W. B. Cairncross, J. T. Zhang, L. R. B. Picard, Y. Yu, K. Wang, and K.-K. Ni, Phys. Rev. Lett. **126**, 123402 (2021).
[90] J. Wei, P. Li, J. Wu, V. Sovkov, W. Liu, Y. Li, Y. Fu, F. Xie, and J. Ma, Phys. Rev. A **105**, 063322 (2022).
[91] S. H. Yuwono, I. Magoulas, and P. Piecuch, Sci. Adv. **6**, eaay4058 (2020).
[92] B. Helmich-Paris, M. Repisky, and L. Visscher, Chem. Phys. **518**, 38 (2019).
[93] S. Banerjee, T. Zhang, K. G. Dyall, and X. Li, J. Chem. Phys. **159**, 114119 (2023).
[94] C. Zhang, F. Lipparini, S. Stopkowicz, J. Gauss, and L. Cheng, J. Chem. Theory Comput. **20**, 787 (2024).
[95] S. Chamoli, K. Surjuse, B. Jangid, M. K. Nayak, and A. K. Dutta, J. Chem. Phys. **156**, 204120 (2022).
[96] X. Yuan, L. Visscher, and A. S. P. Gomes, J. Chem. Phys. **156**, 224108 (2022).
[97] K. Surjuse, S. Chamoli, M. K. Nayak, and A. K. Dutta, J. Chem. Phys. **157**, 204106 (2022).